PHYSICS

Attosecond timing of electron emission from a molecular shape resonance

S. Nandi[1,2]*[†], E. Plésiat[3]*, S. Zhong[1]*, A. Palacios[3,4], D. Busto[1], M. Isinger[1], L. Neoričić[1], C. L. Arnold[1], R. J. Squibb[5], R. Feifel[5], P. Decleva[6], A. L'Huillier[1], F. Martín[3,7,8,9], M. Gisselbrecht[1]

Shape resonances in physics and chemistry arise from the spatial confinement of a particle by a potential barrier. In molecular photoionization, these barriers prevent the electron from escaping instantaneously, so that nuclei may move and modify the potential, thereby affecting the ionization process. By using an attosecond two-color interferometric approach in combination with high spectral resolution, we have captured the changes induced by the nuclear motion on the centrifugal barrier that sustains the well-known shape resonance in valence-ionized N_2. We show that despite the nuclear motion altering the bond length by only 2%, which leads to tiny changes in the potential barrier, the corresponding change in the ionization time can be as large as 200 attoseconds. This result poses limits to the concept of instantaneous electronic transitions in molecules, which is at the basis of the Franck-Condon principle of molecular spectroscopy.

INTRODUCTION

Shape resonances, due to trapping of particles in potential barriers, are ubiquitous in nature. First discovered by Fermi *et al.* when studying slow-neutron capture in artificial radioactivity (*1*, *2*), they have since been the focus of countless investigations in physics, chemistry, and biology. They play a crucial role in α-decay of radioactive nuclei (*3*), molecular fragmentation (*4*), rotational predissociation (*5*), electron detachment (*6*), ultracold collisions (*7*), low-energy electron scattering (*8*, *9*), and photoionization (*10*, *11*), to name a few. They are also thought to be at the origin of enhanced radiation damage of DNA and other biomolecules (*12*) and to play an important role in the stability of Bose-Einstein condensates (*13*). Shape resonances are usually associated to specific spectral features. For instance, they lead to broad peaks in the photoionization spectrum of atoms and molecules (*14–17*) and to a strong variation in the corresponding photoelectron angular distribution as a function of kinetic energy (*18*).

The energies at which these resonances are expected to appear and the corresponding trapping times (or conversely, decay lifetimes) are entirely determined by the shape of the barrier seen by the trapped (or ejected) particle, hence the name "shape resonances." Thus, the analysis of the resonance peaks observed in experimental spectra can be used to infer the actual height and width of the potential barrier seen by the impinging or emitted particle. This can be unambiguously done in atomic systems. However, in molecules, the situation is more complicated, as nuclear motion may cause the potential felt by the electrons to change during a vibrational period, thus affecting the shape of the barrier. This was theoretically predicted back in 1979 by Dehmer, who argued that the anomalous variations of vibrationally resolved photoelectron angular distributions of N_2 with photon energy could be the consequence of changes in the shape of the potential barrier with the internuclear distance (*10*). This prediction has been the subject of debate for years (*11*). So far, direct time-resolved measurements of the dynamical evolution of shape resonances as the molecule vibrates have not been possible due to the lack of temporal resolution.

In this work, we investigate with attosecond time resolution the changes induced by the vibrational motion on the potential barrier that sustains the $3\sigma_g^{-1}$ shape resonance in N_2. We do so by ionizing the molecule with extreme ultraviolet (XUV) radiation consisting of high-order harmonics spanning an energy range between 20 and 40 eV (see Fig. 1A). Temporal information is obtained by using the RABBIT (reconstruction of attosecond beating by interference of two-photon transitions) interferometric method, described below (*19*). In particular, we determine the (relative) photoionization delay, which is the time the electron takes to escape from the molecular potential and is thus sensitive to the presence of a shape resonance. With the support of theoretical calculations that explicitly describe the photoionization process and take into account the vibrational motion, we show that changes in the molecular bond length of only 0.02 Å can lead to variations of the photoionization delay as large as 200 as and are not uniform over the investigated energy range. These measurements with attosecond time resolution show that molecular photoionization in the vicinity of shape resonances cannot be described in terms of the commonly accepted Franck-Condon picture, in which electronic excitation is assumed to be instantaneous and decoupled from the nuclear motion.

RESULTS AND DISCUSSION

The RABBIT technique has been widely used to determine accurate photoionization delays in atoms (*20*, *21*) and, following the pioneering work of Haessler *et al.* (*22*), has started to be applied to molecular systems as well (*23–25*). Here, N_2 is ionized by a comb of odd high-order harmonics, covering the $3\sigma_g^{-1}$ shape resonance (see

[1]Department of Physics, Lund University, 22100 Lund, Sweden. [2]Université de Lyon, Université Claude Bernard Lyon 1, CNRS, Institut Lumière Matière, F-69622 Villeurbanne, France. [3]Departamento de Química, Módulo 13, Universidad Autónoma de Madrid, 28049 Madrid, Spain. [4]Institute of Advanced Research in Chemical Sciences (IAdChem), Universidad Autónoma de Madrid, 28049 Madrid, Spain. [5]Department of Physics, University of Gothenburg, 41296 Göteborg, Sweden. [6]Dipartimento di Scienze Chimiche e Farmaceutiche, Universitá di Trieste and IOM-CNR, 34127 Trieste, Italy. [7]Instituto Madrileño de Estudios Avanzados en Nanociencia (IMDEA-Nanociencia), Cantoblanco, 28049 Madrid, Spain. [8]Condensed Matter Physics Center (IFIMAC), Universidad Autónoma de Madrid, 28049 Madrid, Spain. [9]Donostia International Physics Center (DIPC), Paseo Manuel de Lardizabal 4, 20018 Donostia-San Sebastián, Spain.
*These authors contributed equally to this work.
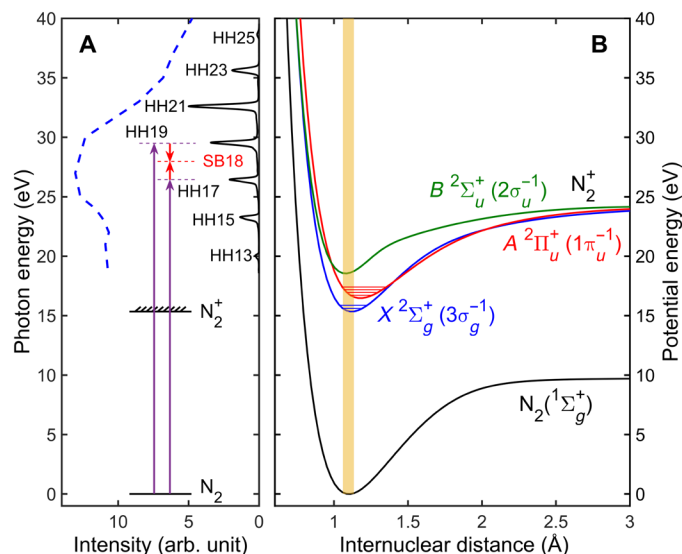†Corresponding author. Email: saikat.nandi@univ-lyon1.fr

Fig. 1. Photoionization scheme. (**A**) A comb of high-order harmonics (HH), spanning over the photon energy range of 20 to 40 eV, probes the entire shape resonance region in N_2^+. The blue dashed line corresponds to experimental photoionization cross sections [taken from (30)] across the resonance. The scheme for generating sideband 18 (SB18) is denoted by the vertical arrows. The violet (red) arrows denote XUV (NIR) photons. (**B**) Potential energy curves of the ground state of N_2: $^1\Sigma_g^+$ (black), and lowest three states of N_2^+: $X\,^2\Sigma_g^+$ (blue), $A\,^2\Pi_u^+$ (red), and $B\,^2\Sigma_u^+$ (green). The shaded area (1.06 to 1.14 Å) denotes the Franck-Condon region. The horizontal lines show the position of different vibrational levels associated with the corresponding electronic state.

Fig. 1A). Electrons are mainly removed from the $3\sigma_g$ and $1\pi_u$ orbitals of the N_2 molecule in its $^1\Sigma_g^+$ ground state, leading to N_2^+ ions in the $X\,^2\Sigma_g^+$ and $A\,^2\Pi_u^+$ states (X and A states for short), respectively (see Fig. 1B).

In our experiment (see Materials and Methods for details), a near-infrared (NIR) 45-fs laser pulse generated high-order harmonics in argon, corresponding to a train of attosecond pulses in the time domain (26). The harmonics and a weak replica of the NIR pulse (probe) were focused into an effusive gas jet containing N_2 molecules. The ejected electrons were detected by a magnetic bottle electron spectrometer with a resolution up to $E/\Delta E \sim 80$. To use the best possible resolution and hence resolve the vibrational levels in the first two outer valence states of the N_2^+ ion, we retarded photoelectrons by suitable voltages before entering into the spectrometer flight tube. The measurements consisted in recording, for alternating shots, the XUV-only and XUV + NIR photoelectron spectra (PES) as a function of the delay (τ) between the XUV and NIR pulses.

We perform simulations to explicitly obtain the vibrationally resolved PES resulting from the interaction of an isolated N_2 molecule with an XUV attosecond pulse train and a time-delayed NIR pulse, so that the extracted time delays can be directly compared with experiment. The time-dependent Schrödinger equation is numerically solved including the bound-bound, bound-continuum, and continuum-continuum dipole transition matrix elements between the electronic states. These are computed using the static exchange density functional theory method described in (27). The nuclear motion is taken into account within the Born-Oppenheimer approximation (see the "Theoretical Methods" section in the

Supplementary Materials for a detailed explanation), and the laser parameters are chosen to reproduce the experimental conditions.

The measured and calculated PES, obtained with XUV and NIR, exhibit sidebands originating from the interference between two quantum paths: the absorption of a harmonic and an NIR photon and the absorption of the next harmonic and the stimulated emission of an NIR photon (see Fig. 1A). Consequently, the amplitude of the sidebands, A_{SB}, oscillates as a function of τ according to the formula (19)

$$A_{SB} = \mathcal{A} + \mathcal{B}\cos\left[2\omega_0(\tau - \tau_{XUV} - \tau_{mol})\right] \quad (1)$$

where $\mathcal{A}$ and $\mathcal{B}$ are two constants, ω_0 is the angular frequency of the driving NIR field, τ_{XUV} denotes the group delay of the attosecond pulses (28), and τ_{mol} is the molecular two-photon ionization time delay (see the Supplementary Materials) (29). The combination of both high spectral and temporal resolution achieved in our experiment allows us to distinguish photoelectrons leaving the residual molecular cation in different vibrational states and to determine the variation in photoionization delays due to changes in the molecular geometry.

Figure 2 (A and B) shows the experimental and theoretical data, respectively, corresponding to the difference between the XUV + NIR and XUV-only PES (in color), which oscillates with frequency $2\omega_0$ as a function of τ. Both theory and experiment are in excellent agreement (for details about the theoretical method, see the Supplementary Materials). Figure 2C presents the XUV-only (violet) and XUV + NIR (black) PES obtained by integrating over all delays. Good agreement with the calculated spectra shown in Fig. 2D can be noticed. The difference between theory and experiment in the relative intensities of some of the photoelectron peaks is due to the different position of the shape resonance predicted by theory (see Fig. 3B). In addition, the harmonic comb used in the theoretical calculations was slightly different from the experimental one. Figure 2E presents individual contributions from the X (blue) and A (red) states in the theoretical XUV + NIR PES, which allows us to assign the different features of the experimental spectra. The structures between 14.5 and 16 eV, for example, are due to ionization to the A state by absorption of the 21st harmonic leaving the N_2^+ ion in the $v' = 0 - 6$ vibrational states and to a two-photon transition (sideband) to the X state with vibrational states $v' = 0,1$ (blue shaded region). The small peaks near 14 eV are due to two-photon transitions to the A state with vibrational states $v' = 0,1$ (red shaded region). Plotting the difference between the XUV + NIR and XUV-only PES allows us to confirm our assignment, since, as shown in Fig. 2A, we can distinguish between sideband (positive) and harmonic (negative) peaks.

To determine molecular two-photon ionization time delays τ_{mol}, we fitted the measured (Fig. 2A) sideband oscillations to Eq. 1. The same procedure is applied to extract the theoretical ones from the RABBIT spectra computed with a time-dependent numerical approach. Figure 3 (A, C, and D) shows experimental (red circles) and theoretical (black circles) relative time delays for different final states. Since the contribution from the ionizing radiation (τ_{XUV}) is the same for all the final states of N_2^+, the plotted differences correspond to pure molecular contributions.

The relative molecular time delay for leaving N_2^+ in the $X(v' = 0)$ state with respect to leaving it in the $A(v' = 0)$ state is shown in
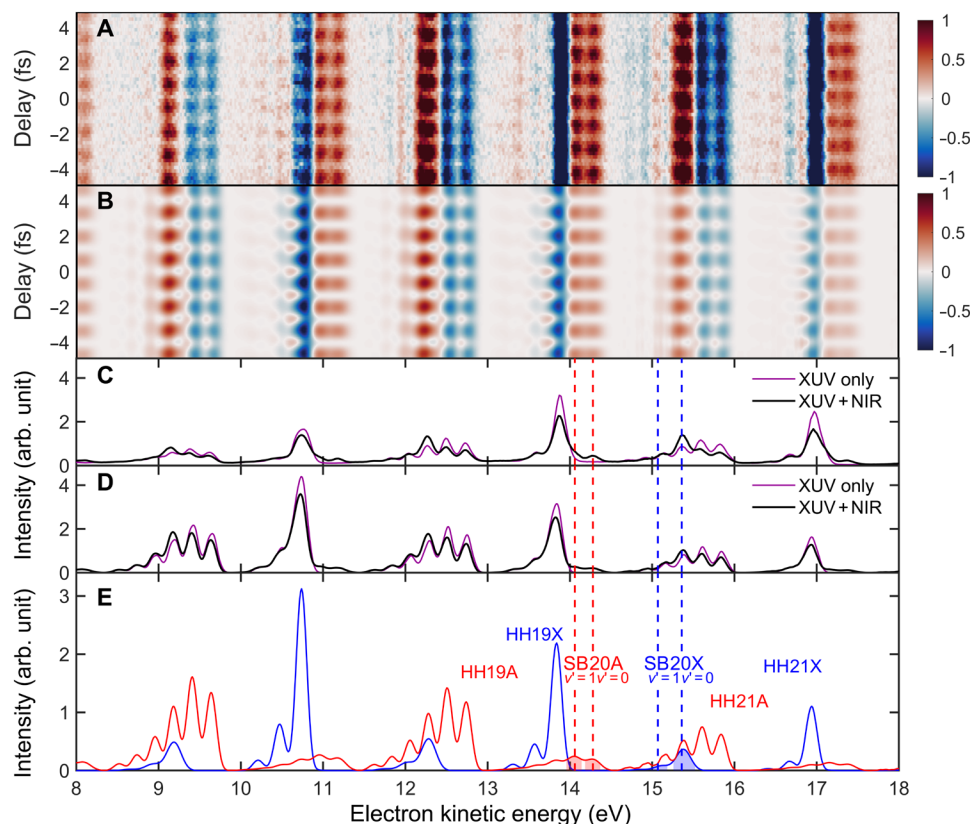
Fig. 2. Photoelectron spectra. Difference between PES obtained with XUV + NIR and XUV only, as a function of delay. Experiment (**A**) and theory (**B**). Experimental (**C**) and theoretical (**D**) PES for XUV-only (violet) and XUV + NIR (black) photoionization, averaged over all relative delays. (**E**) Theoretical PES for XUV + NIR photoionization to the X (blue) and A (red) electronic states. By comparing (A) and (E), we can assign the spectral features to different vibrational levels (shaded areas) of the X and A electronic states, as indicated by the vertical blue and red dashed lines, respectively.

Fig. 3A. For both theory and experiment, this relative delay varies by more than 40 as across the shape resonance region. The theoretical results, however, are shifted to lower energies with respect to the experimental ones by almost 6 eV, indicated by the green arrow in Fig. 3A, which is similar to the shift of the maximum of the calculated photoionization cross section in comparison with that obtained from synchrotron radiation measurements (see Fig. 3B) (*30*, *31*). This is due to an incorrect description of the resonance position by our theoretical method, which is necessarily simpler than state-of-the-art electronic structure methods for the equilibrium geometry (*32*), as we must describe the molecular electronic continuum states in a wide range of internuclear distances, as well as all the continuum-continuum transitions induced by the NIR probe pulse (see the Supplementary Materials).

Figure 3 (C and D) shows the relative molecular time delays, $\tau_X(v' = 1) - \tau_X(v' = 0)$ and $\tau_A(v' = 1) - \tau_A(v' = 0)$, for the X and A electronic states, respectively. For the A state, the relative delay is very small and practically independent of photon energy, while for the X state, it varies markedly across the shape resonance. Once again, for the reasons described above, the theoretical curve is shifted down in energy with respect to the experimental one by ~6 eV.

The variation of the molecular time delay differences between the X and A states observed in Fig. 3A is therefore mainly due to the variation of the time delay for the former, which can be attributed to the presence of the shape resonance. The time delay varies with

energy because the time spent by the photoelectron in the metastable state before being ejected into the continuum also varies with energy. Since, for the A state, the electron does not have to go through any potential barrier, the corresponding time delay is much smaller than for the X state.

We now analyze the physical meaning of the results presented in Fig. 3 (C and D). In atomic systems, photoionization time delays obtained from RABBIT measurements can often be written as the sum of two contributions, $\tau_1 + \tau_{cc}$. The first term is related to one-photon ionization by the XUV field. For a single or dominant ionization channel containing no sharp structures in the continuum (e.g., narrow Fano resonances), τ_1 is given by the derivative of the scattering phase in that particular channel, the so-called Wigner delay (*33*, *34*). The second term, τ_{cc}, is the additional time delay due to the continuum-continuum transitions induced by the NIR field (*35*, *36*).

In the vicinity of the shape resonance, one-photon ionization leading to N_2^+ in the X state is dominated by the f-wave ($\ell = 3$). Similarly, for the A state, the d-wave ($\ell = 2$) dominates over all other partial waves in the same photon energy region (see fig.S2). Although the molecular two-photon ionization time delay τ_{mol} cannot be strictly decomposed as $\tau_1 + \tau_{cc}$, due to averaging over molecular orientation and electron emission angle, the variation of τ_{mol} in Fig. 3 (C and D) still reflects the ionization dynamics arising from the main channels (*29*). Figure 4 shows the modulus and phase of
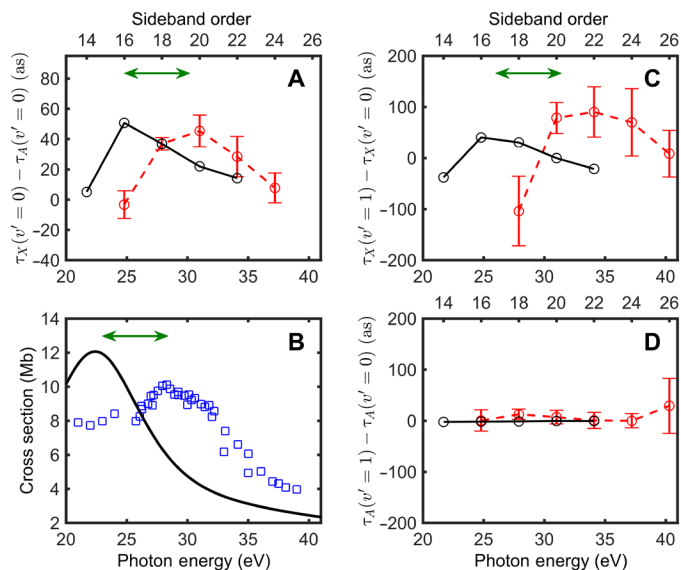
Fig. 3. Photoionization time delays. (**A**) Differences in molecular time delays (τ_{mol}) between X and A states for $v' = 0$. Red circles, experiment; black circles, theory. (**B**) Partial photoionization cross sections for the X state; open squares, synchrotron-based experiment (*30, 31*); solid line, theory (this work). The position of the resonance maxima is shifted by almost 6 eV (denoted as ↔) between theory and experiment. This shift is also observed in the relative time delay (A and C). (**C**) Relative time delay between the vibrational levels $v' = 1$ and 0 for the X state. The strong photon energy dependence observed here vanishes completely if one neglects the nuclear motion (see fig. S4). (**D**) Same as (C), but for the A state.

Fig. 4. One-photon dipole transition matrix elements. Modulus (**A** and **C**) and phase (**B** and **D**) of the dominant terms $d^X_{\sigma_u, l=3, z}$ (A and B) and $d^A_{\delta_g, l=2, x}$ (C and D) contributing to the one-photon transition matrix element of the X and A states, respectively, as a function of the internuclear distance (R) and electron kinetic energy (ε). The area between the two dashed lines denotes the Franck-Condon region.

the dominant terms contributing to the dipole transition element as a function of electron kinetic energy ε and internuclear distance R for both electronic states (see the Supplementary Materials for notations). For the X state, at a given ε, both the modulus (Fig. 4A) and phase (Fig. 4B) of the dipole transition element strongly vary with R within the Franck-Condon region, in contrast to the A state (Fig. 4, C and D). This implies that electronic transitions cannot be considered instantaneous relative to nuclear motion as assumed by the widely used Franck-Condon picture. Consequently, the molecular photoionization delays, obtained by taking the derivative of the phase of the dipole transition element, strongly depend on R. The difference in molecular time delays between the $v' = 1$ and 0 vibrational levels thus provides direct information on non–Franck-Condon ionization dynamics, i.e., on how the nuclear motion affects the photoionization process.

Figure 5A shows the absolute square of the product between the initial vibrational wave function, the transition matrix element for the X state (see Fig. 4A) at an electron kinetic energy of 8.2 eV, and the final vibrational wave function (see the Supplementary Materials for details). The initial and final vibrational wave functions correspond, respectively, to the $v = 0$ level of N_2 in the ground electronic state and the $v' = 0$ (black) and $v' = 1$ (red) levels of N_2^+ in the X electronic state. These curves have well-defined maxima at $R = 1.113$ and 1.09 Å, respectively, showing that the transition to the shape resonance occurs, on average, at smaller internuclear distances for $v' = 1$ than for $v' = 0$. This small difference in bond length of ~0.02 Å has a notable impact on the electron dynamics. As illustrated in Fig. 5B, the potential felt by the emitted photoelectron at these two internuclear distances is different, leading to a
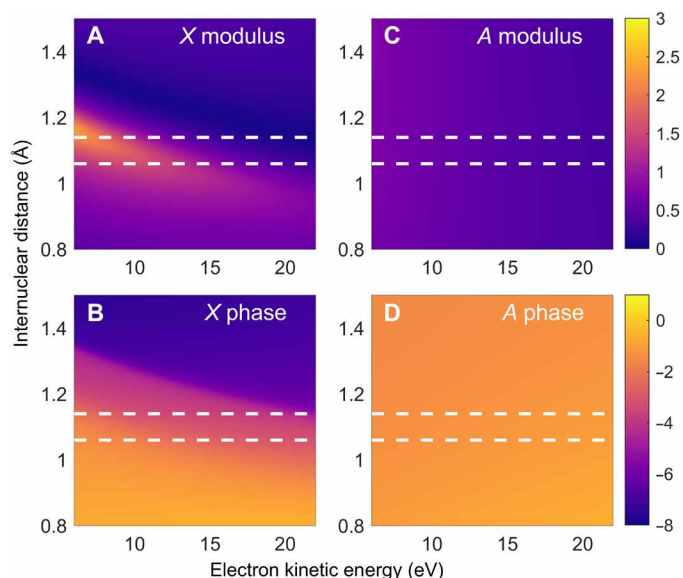
higher resonance energy for $R = 1.09$ Å ($v' = 1$) than for $R = 1.113$ Å ($v' = 0$), as seen by comparing the red and black dashed lines. In addition, because of the different slopes on the rising (left inset in Fig. 5B) and falling (right inset in Fig. 5B) edges, the barrier is narrower, and the resonance lifetime is shorter for $v' = 1$ than for $v' = 0$.

Figure 5C shows the photoionization delays resulting from the one-photon dipole transition matrix elements calculated at the two abovementioned internuclear distances as a function of photon energy. The difference in internuclear distance leads to a noticeable shift in the position of the corresponding maxima of photoionization delays, in agreement with the difference in resonance energy discussed above and the positions of the maxima calculated using the Wentzel-Kramers-Brillouin (WKB) approximation, indicated by the black and red dots. In addition, the energy range where the photoionization delays vary substantially is slightly broader for $v' = 1$ than for $v' = 0$, a direct consequence of the shorter lifetime for $v' = 1$. This can also be seen by the horizontal bars, representing the widths of resonance obtained with the WKB approximation. Both effects, due to the shape resonance, contribute to a variation of the time delay difference between the $v' = 1$ and $v' = 0$ states as indicated by the green curve. Such a simple model predicts the main features of the experimental results in Fig. 3C, particularly the change of sign of the relative photoionization delay at low photon energy and the maximum at approximately the resonance position. It is worth noting that the resonance lifetimes obtained from the WKB model, 139.6 and 163 as for the $v' = 1$ and $v' = 0$ levels, respectively, are much smaller than the corresponding vibrational period, which is of the order of 16 fs (see the Supplementary Materials for details). As a consequence, the nuclei barely move during the ionization process, thus supporting the above analysis.
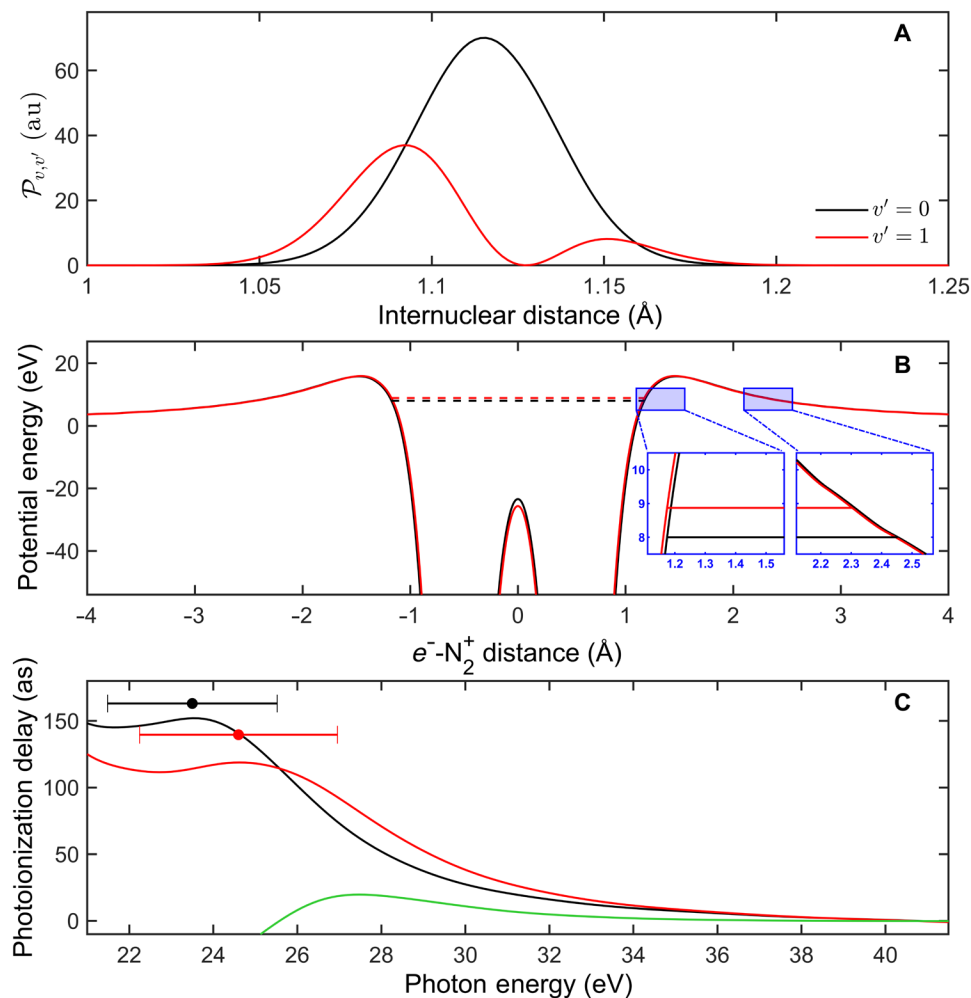
Fig. 5. Electron dynamics induced by structural changes. (**A**) Absolute square of the transition matrix element $d_{\sigma_u, l=3, z}^X$ at an electron kinetic energy of 8.2 eV, multiplied by the initial ($\chi_{i;v=0}$) and final ($\chi_{f,v'}$) vibrational wave functions, $\mathcal{P}_{v,v'}$, as a function of the internuclear distance R. The red and black curves correspond to transitions from the $v = 0$ level in the neutral ground state to the $v' = 1$ and the $v' = 0$ levels of the X state, respectively. (**B**) Potential felt by an electron escaping from an N_2 molecule with internuclear distance $R_{v'=1} = 1.09$ Å (red) and $R_{v'=0} = 1.113$ Å (black), calculated at the same of level of theory as the dipole matrix elements. These Kohn-Sham potentials are shown along the internuclear axis, with the two wells representing the two N atoms. The origin is placed at the center of mass of the molecular ion. The dashed lines show the corresponding resonance energies. As shown in the insets, the barrier width depends on R, hence, on the vibrational state of the ion. Figure 5C shows the photoionization delays (τ_1) as a function of photon energy obtained at the internuclear distances $R_{v'=1} = 1.09$ Å (red) and $R_{v'=0} = 1.113$ Å (black) and the relative delay between them, $\tau_1^X(R_{v'=1}) - \tau_1^X(R_{v'=0})$ (green). The resonance lifetimes (full circles) and widths (horizontal bar) calculated in the Wentzel-Kramers-Brillouin (WKB) approximation from the two potentials presented in Fig. 5B are also shown.

CONCLUSION

In summary, we measured vibrationally resolved molecular photoionization time delays between the X and A electronic states in N_2 across the $3\sigma_g^{-1}$ shape resonance using attosecond interferometry. This enabled us to capture the changes associated with nuclear motion on the centrifugal barrier seen by the escaping photoelectron. The observation of such changes goes beyond the usual Franck-Condon approximation, which assumes that electronic transitions are instantaneous in comparison with nuclear motion. By combining attosecond time resolution with high spectral resolution, we were able to break the temporal frontier beyond which the signature of the "slow" nuclear motion in molecular photoionization can be seen and quantified. This approach should allow investigating the effect of nuclear motion on a variety of electronic

processes in more complex molecular systems at the subfemtosecond time scale.

MATERIALS AND METHODS
Experimental methods

The output of a Ti:Sapphire laser system delivering NIR pulses around 800 nm with 5-mJ pulse energy at 1-kHz repetition rate was sent to an actively stabilized Mach-Zehnder–type interferometer. In the "pump" arm, the NIR pulses were focused into a gas cell containing argon atoms to produce a train of attosecond XUV pulses via high-order harmonic generation. A 200-nm-thick aluminum foil was used to filter out the copropagating NIR pulse. The bandwidth of the driving NIR pulse was kept around 50 nm, which

ensured the generation of high-order harmonics having full width at half maximum of about 150 meV. This is notably smaller than the energy separation (267 meV) between the lowest vibrational levels ($v' = 1$ and $v' = 0$) of the X electronic state in N_2^+ (see the Supplementary Materials), which is essential to vibrationally resolve the measured PES. In the "probe" arm, the NIR pulses could be delayed relative to the XUV pulses by a piezoelectric-controlled delay stage and blocked at each alternate shot by a mechanical chopper. After recombination, the collinearly propagating XUV and NIR pulses were focused by a toroidal mirror into an effusive gas jet of N_2. The emitted photoelectrons were detected by a 2-m-long magnetic bottle electron spectrometer, with a 4π solid angle collection. We estimated an average NIR intensity of 8×10^{11} W/cm^2 in the interaction region.

Data analysis

Because of the spectral congestion between ionization by XUV and XUV + NIR radiation to the three different states (X, A, and B) of the N_2^+ ion (see fig. S1), a careful analysis of the experimental data was needed. Hence, a spectrally resolved variant of the RABBIT protocol, called Rainbow RABBIT (37), was used to analyze the experimental data. Despite the overlap between the X and B states, we could determine the phases of the sideband oscillations by carefully choosing the region with least possible spectral overlap. In addition, at relatively high photon energies (>25 eV), the photoionization cross section to the B state is much smaller than to the X state (29). Therefore, the measured time delays for the X state can be considered to be effectively free from any possible spectral contamination from the B state.

For every sideband, a Fourier transform was performed to make sure that the sideband oscillation did not include frequency components higher than $2\omega_0$. The uncertainty σ_X (σ_A) for each measurement of the molecular photoionization time delay τ_X (τ_A) was obtained from the fit of the RABBIT oscillation to a cosine function (see Eq. 1). The corresponding uncertainty on the relative time delay, $\tau_X - \tau_A$, can be expressed as

$$\sigma_{X-A} = \sqrt{\sigma_X^2 + \sigma_A^2} \quad (2)$$

An identical procedure was used to calculate the uncertainties for the relative time delays between two vibrational levels of the same electronic state.

The final experimental values shown in Fig. 3 were obtained from a weighted average of the data points from several sets of measurements. For N measurements yielding N data points: $k_1, k_2, \ldots, k_N$ with corresponding uncertainties: $\sigma_1, \sigma_2, \ldots, \sigma_N$, the weighted average can be calculated as

$$\bar{k} = \frac{\sum_{i=1}^{N} w_i k_i}{\sum_{i=1}^{N} w_i} \quad (3)$$

where $w_i = 1/\sigma_i^2$ is the weight. The error bars indicated in Fig. 3 are the weighted standard deviation, defined as

$$\sigma_{\bar{k}} = \sqrt{\frac{N \sum_{i=1}^{N} w_i (k_i - \bar{k})^2}{(N-1) \sum_{i=1}^{N} w_i}} \quad (4)$$

SUPPLEMENTARY MATERIALS

REFERENCES AND NOTES

1. E. Fermi, E. Amaldi, O. D'Agostino, F. Rasetti, E. Segrè, Artificial radioactivity produced by neutron bombardment. *Proc. R. Soc. A* **146**, 483–500 (1935).
2. N. Bohr, Neutron capture and nuclear constitution. *Nature* **137**, 344–348 (1936).
3. J. M. Blatt, V. F. Weisskopf, *Theoretical Nuclear Physics* (Springer-Verlag, New York Inc., 1979).
4. W. C. Stolte, D. L. Hansen, M. N. Piancastelli, I. Dominguez Lopez, A. Rizvi, O. Hemmers, H. Wang, A. S. Schlachter, M. S. Lubell, D. W. Lindle, Anionic photofragmentation of CO: A selective probe of core-level resonances. *Phys. Rev. Lett.* **86**, 4504–4507 (2001).
5. C. M. Lovejoy, D. J. Nesbitt, Mode specific internal and direct rotational predissociation in HeHF, HeDF, and HeHCl: van der Waals complexes in the weak binding limit. *J. Chem. Phys.* **93**, 5387–5407 (1990).
6. L. H. Andersen, P. Hvelplund, D. Kella, P. H. Mokler, H. B. Pedersen, H. T. Schmidt, L. Vejby-Christensen, Resonance structure in the electron-impact detachment cross section of C_2^- caused by the formation of C_2^{2-}. *J. Phys. B Atom. Mol. Opt. Phys.* **29**, L643–L649 (1996).
7. A. B. Henson, S. Gersten, Y. Shagam, J. Narevicius, E. Narevicius, Observation of resonances in Penning ionization reactions at sub-kelvin temperatures in merged beams. *Science* **338**, 234–238 (2012).
8. G. J. Schulz, Resonances in electron impact on atoms. *Rev. Mod. Phys.* **45**, 378–422 (1973).
9. R. E. Palmer, P. J. Rous, Resonances in electron scattering by molecules on surfaces. *Rev. Mod. Phys.* **64**, 383–440 (1992).
10. J. L. Dehmer, D. Dill, S. Wallace, Shape-resonance-enhanced nuclear-motion effects in molecular photoionization. *Phys. Rev. Lett.* **43**, 1005–1008 (1979).
11. M. N. Piancastelli, The neverending story of shape resonances. *J. Electron Spectrosc. Relat. Phenom.* **100**, 167–190 (1999).
12. F. Martin, P. D. Burrow, Z. Cai, P. Cloutier, D. Hunting, L. Sanche, DNA strand breaks induced by 0–4 eV electrons: The role of shape resonances. *Phys. Rev. Lett.* **93**, 068101 (2004).
13. X.-C. Yao, R. Qi, X.-P. Liu, X.-Q. Wang, Y.-X. Wang, Y.-P. Wu, H.-Z. Chen, P. Zhang, H. Zhai, Y.-A. Chen, J.-W. Pan, Degenerate Bose gases near a d-wave shape resonance. *Nat. Phys.* **15**, 570–576 (2019).
14. J. B. West, A. C. Parr, B. E. Cole, D. L. Ederer, R. Stockbauer, J. L. Dehmer, Shape-resonance-induced non-Franck-Condon vibrational intensities in $3\sigma_g$ photoionisation of N_2. *J. Phys. B Atom. Mol. Opt. Phys.* **13**, L105–L108 (1980).
15. J. L. Dehmer, Shape resonances in molecular fields. *ACS Symp. Ser.* **263**, 139–163 (1984).
16. N. Haack, G. Ceballos, H. Wende, K. Baberschke, D. Arvanitis, A. L. Ankudinov, J. J. Rehr, Shape resonances of oriented molecules: Ab initio theory and experiment on hydrocarbon molecules. *Phys. Rev. Lett.* **84**, 614–617 (2000).
17. E. Plésiat, S. E. Canton, J. D. Bozek, P. Decleva, F. Martín, Resonant photoelectron confinement in the SF_6 molecule. *J. Phys. Chem. A* **123**, 1062–1068 (2019).
18. J. Adachi, K. Hosaka, S. Furuya, K. Soejima, M. Takahashi, A. Yagishita, S. K. Semenov, N. A. Cherepkov, Shape-resonance-enhanced vibrational effects in the angular distributions of C 1s photoelectrons from fixed-in-space CO molecules. *Phys. Rev. Lett.* **91**, 163001 (2003).
19. P. M. Paul, E. S. Toma, P. Breger, G. Mullot, F. Augé, P. Balcou, H. G. Muller, P. Agostini, Observation of a train of attosecond pulses from high harmonic generation. *Science* **292**, 1689–1692 (2001).
20. K. Klünder, J. M. Dahlström, M. Gisselbrecht, T. Fordell, M. Swoboda, D. Guénot, P. Johnsson, J. Caillat, J. Mauritsson, A. Maquet, R. Taïeb, A. L'Huillier, Probing single-photon ionization on the attosecond time scale. *Phys. Rev. Lett.* **106**, 143002 (2011).
21. M. Isinger, R. J. Squibb, D. Busto, S. Zhong, A. Harth, D. Kroon, S. Nandi, C. L. Arnold, M. Miranda, J. M. Dahlström, E. Lindroth, R. Feifel, M. Gisselbrecht, A. L'Huillier, Photoemission in the time and frequency domain. *Science* **358**, 893–896 (2017).
22. S. Haessler, B. Fabre, J. Higuet, J. Caillat, T. Ruchon, P. Breger, B. Carré, E. Constant, A. Maquet, E. Mével, P. Salières, R. Taïeb, Y. Mairesse, Phase-resolved attosecond near-threshold photoionization of molecular nitrogen. *Phys. Rev. A* **80**, 011404(R) (2009).
23. M. Huppert, I. Jordan, D. Baykusheva, A. von Conta, H. J. Wörner, Attosecond delays in molecular photoionization. *Phys. Rev. Lett.* **117**, 093001 (2016).
24. L. Cattaneo, J. Vos, R. Y. Bello, A. Palacios, S. Heuser, L. Pedrelli, M. Lucchini, C. Cirelli, F. Martín, U. Keller, Attosecond coupled electron and nuclear dynamics in dissociative ionization of H_2. *Nat. Phys.* **14**, 733–738 (2018).

25. J. Vos, L. Cattaneo, S. Patchkovskii, T. Zimmermann, C. Cirelli, M. Lucchini, A. Kheifets, A. S. Landsman, U. Keller, Orientation-dependent stereo Wigner time delay and electron localization in a small molecule. *Science* **360**, 1326–1330 (2018).

26. P. Antoine, A. L'Huillier, M. Lewenstein, Attosecond pulse trains using high-order harmonics. *Phys. Rev. Lett.* **77**, 1234–1237 (1996).

27. E. Plésiat, M. Lara-Astiaso, P. Decleva, A. Palacios, F. Martín, Real-time imaging of ultrafast charge dynamics in tetrafluoromethane from attosecond pump-probe photoelectron spectroscopy. *Chem. A Eur. J.* **28**, 12061–12070 (2018).

28. Y. Mairesse, A. de Bohan, L. J. Frasinski, H. Merdji, L. C. Dinu, P. Monchicourt, P. Breger, M. Kovačev, R. Taïeb, B. Carré, H. G. Muller, P. Agostini, P. Salières, Attosecond synchronization of high-harmonic soft X-rays. *Science* **302**, 1540–1543 (2003).

29. D. Baykusheva, H. J. Wörner, Theory of attosecond delays in molecular photoionization. *J. Chem. Phys.* **146**, 124306 (2017).

30. A. Hamnett, W. Stoll, C. E. Brion, Photoelectron branching ratios and partial ionization cross-sections for CO and N_2 in the energy range 18–50 eV. *J. Electron Spectrosc. Relat. Phenom.* **8**, 367–376 (1976).

31. E. W. Plummer, T. Gustafsson, W. Gudat, D. E. Eastman, Partial photoionization cross sections of N_2 and CO using synchrotron radiation. *Phys. Rev. A* **15**, 2339–2355 (1977).

32. E. Plésiat, P. Decleva, F. Martín, Vibrational branching ratios in the photoelectron spectra of N_2 and CO: Interference and diffraction effects. *Phys. Chem. Chem. Phys.* **14**, 10853–10871 (2012).

33. E. P. Wigner, Lower limit for the energy derivative of the scattering phase shift. *Phys. Rev.* **98**, 145–147 (1955).

34. F. T. Smith, Lifetime matrix in collision theory. *Phys. Rev.* **118**, 349–356 (1960).

35. J. M. Dahlström, D. Guénot, K. Klünder, M. Gisselbrecht, J. Mauritsson, A. L'Huillier, A. Maquet, R. Taïeb, Theory of attosecond delays in laser-assisted photoionization. *Chem. Phys.* **414**, 53–64 (2013).

36. J. M. Dahlström, A. L'Huillier, A. Maquet, Introduction to attosecond delays in photoionization. *J. Phys. B Atom. Mol. Opt. Phys.* **45**, 183001 (2012).

37. V. Gruson, L. Barreau, Á. Jiménez-Galan, F. Risoud, J. Caillat, A. Maquet, B. Carré, F. Lepetit, J.-F. Hergott, T. Ruchon, L. Argenti, R. Taïeb, F. Martín, P. Salières, Attosecond dynamics through a Fano resonance: Monitoring the birth of a photoelectron. *Science* **354**, 734–738 (2016).

38. L. S. Cederbaum, Born-Oppenheimer approximation and beyond for time-dependent electronic processes. *J. Chem. Phys.* **128**, 124101 (2008).

39. M. Stener, D. Toffoli, G. Fronzoni, P. Decleva, Recent advances in molecular photoionization by density functional theory based approaches. *Theor. Chem. Acc.* **117**, 943–956 (2006).

40. H. J. Ludde, A. Macfas, F. Martín, A. Riera, J. L. Sanz, Inclusive cross sections in collisions of multicharged ions with dressed targets. *J. Phys. B Atom. Mol. Opt. Phys.* **28**, 4101–4115 (1995).

41. R. van Leeuwen, E. J. Baerends, Exchange-correlation potential with correct asymptotic behavior. *Phys. Rev. A* **49**, 2421–2431 (1994).

42. R. Pazourek, S. Nagele, J. Burgdörfer, Attosecond chronoscopy of photoemission. *Rev. Mod. Phys.* **87**, 765–802 (2015).

Citation: S. Nandi, E. Plésiat, S. Zhong, A. Palacios, D. Busto, M. Isinger, L. Neoričić, C. L. Arnold, R. J. Squibb, R. Feifel, P. Decleva, A. L'Huillier, F. Martín, M. Gisselbrecht, Attosecond timing of electron emission from a molecular shape resonance. *Sci. Adv.* **6**, eaba7762 (2020).